# Supporting Information

## Impact of atomic layer deposited TiO$_2$ on the photocatalytic efficiency of TiO$_2$/w-VA-CNTs nanocomposite materials

Inês E. Oliveira[a, c, d], Ricardo M. Silva[a], J. Rodrigues[b], M. R. Correia[b], T. Monteiro[b], Joaquim L. Faria[c, d], Rui F. Silva[a], Cláudia G. Silva*[c, d]

[a] CICECO - Aveiro Institute of Materials, Department of Materials and Ceramic Engineering, University of Aveiro, 3810-193 Aveiro, Portugal.

[b] i3N, Department of Physics, University of Aveiro, 3810-193 Aveiro, Portugal.

[c] LSRE-LCM - Laboratory of Separation and Reaction Engineering – Laboratory of Catalysis and Materials, Faculty of Engineering, University of Porto, Rua Dr. Roberto Frias s/n, 4200-465 Porto, Portugal.

[d] ALiCE - Associate Laboratory in Chemical Engineering, Faculty of Engineering, University of Porto, Rua Dr. Roberto Frias, 4200-465 Porto, Portugal
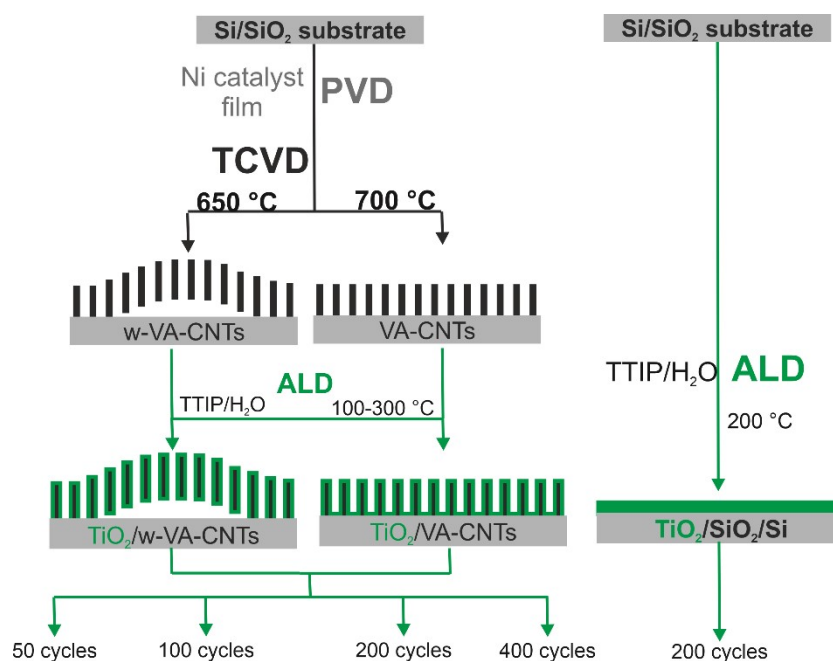
Figure S1. Schematic representation of TiO$_2$ deposited via ALD on 1 cm × 1 cm VA-CNTs with different surface topography and on 1 cm × 1 cm Si/SiO$_2$ substrate for comparison purposes. The photocatalytic activity of these samples was assessed by photodegradation of RhB.
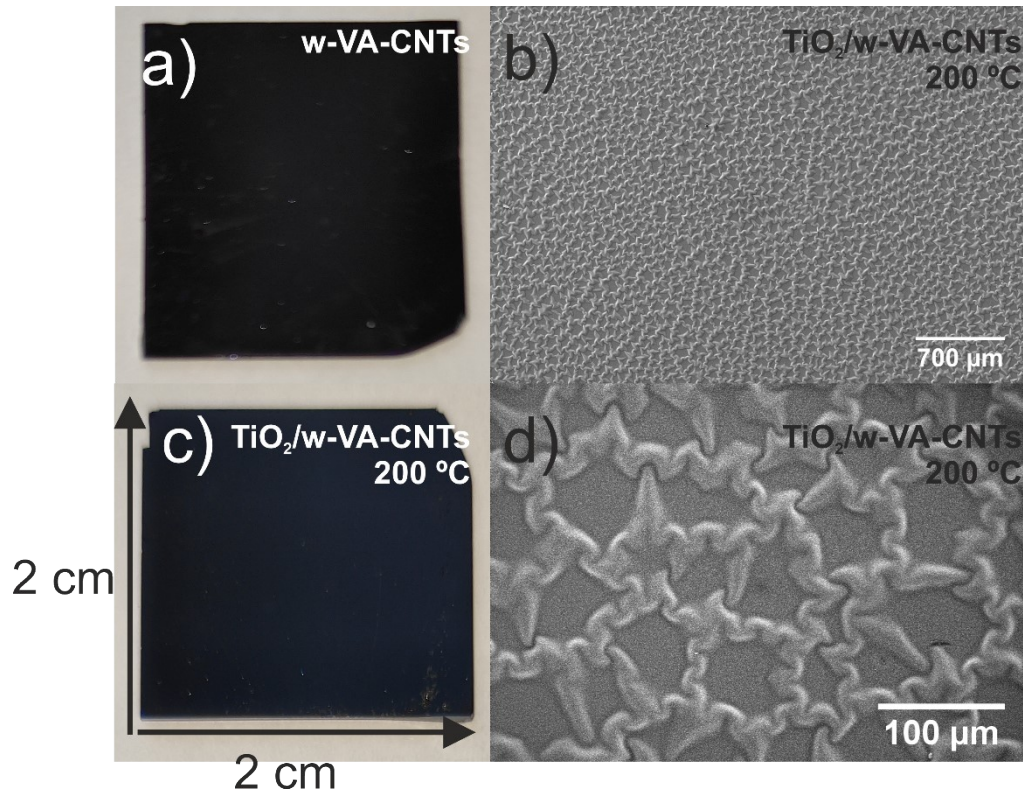
Figure S2. Macrographs of the physical appearance of the VA-CNTs (a) before and (c) after TiO$_2$ ALD, 200 ALD cycles at 200 °C (not to scale). (b) and (d) Top view SEM images of w-VA-CNTs after TiO$_2$ ALD, 200 ALD cycles at 200 °C.



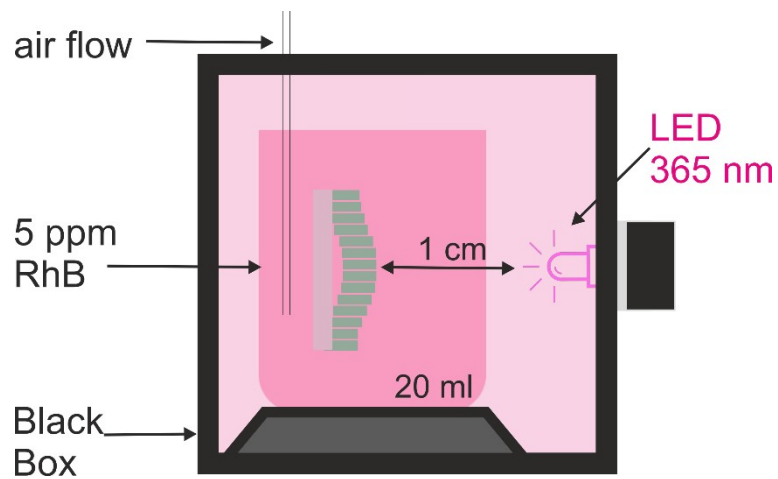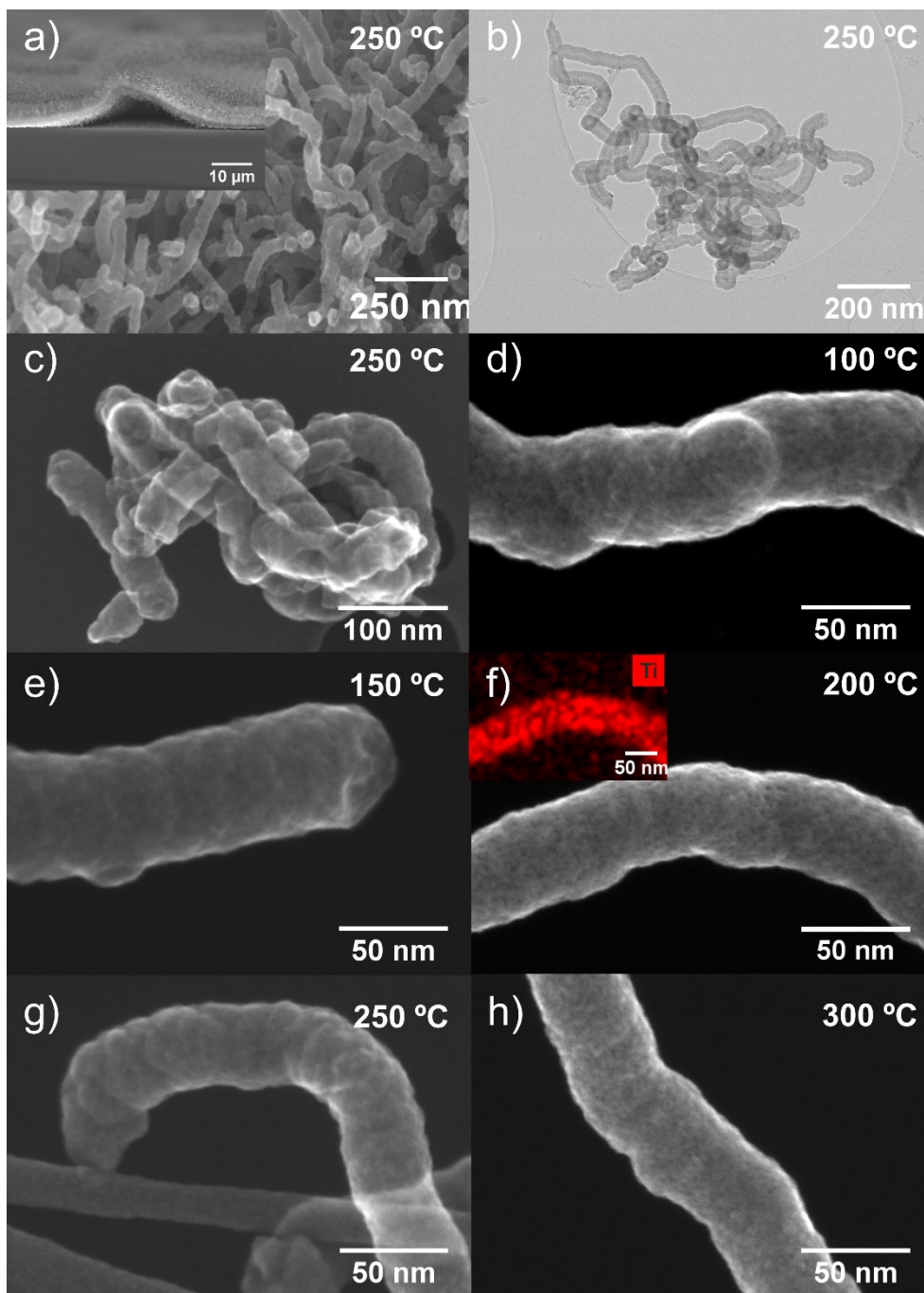Figure S3. Experimental set-up for photocatalytic reactions of RhB.

Figure S4. Low- and high magnification cross-sectional SEM image (a) of the TiO$_2$/w-VA-CNTs nanocomposite after 200 ALD cycles. TE-STEM mode image (b), SE-STEM mode image of the coated CNTs. SE-STEM mode of an individual coated nanotube (c,d,e,f,g,h). The inset in (f) shows the STEM/EDS mapping of Ti on the nanotube surface, elucidating the contrast-based interpretation.
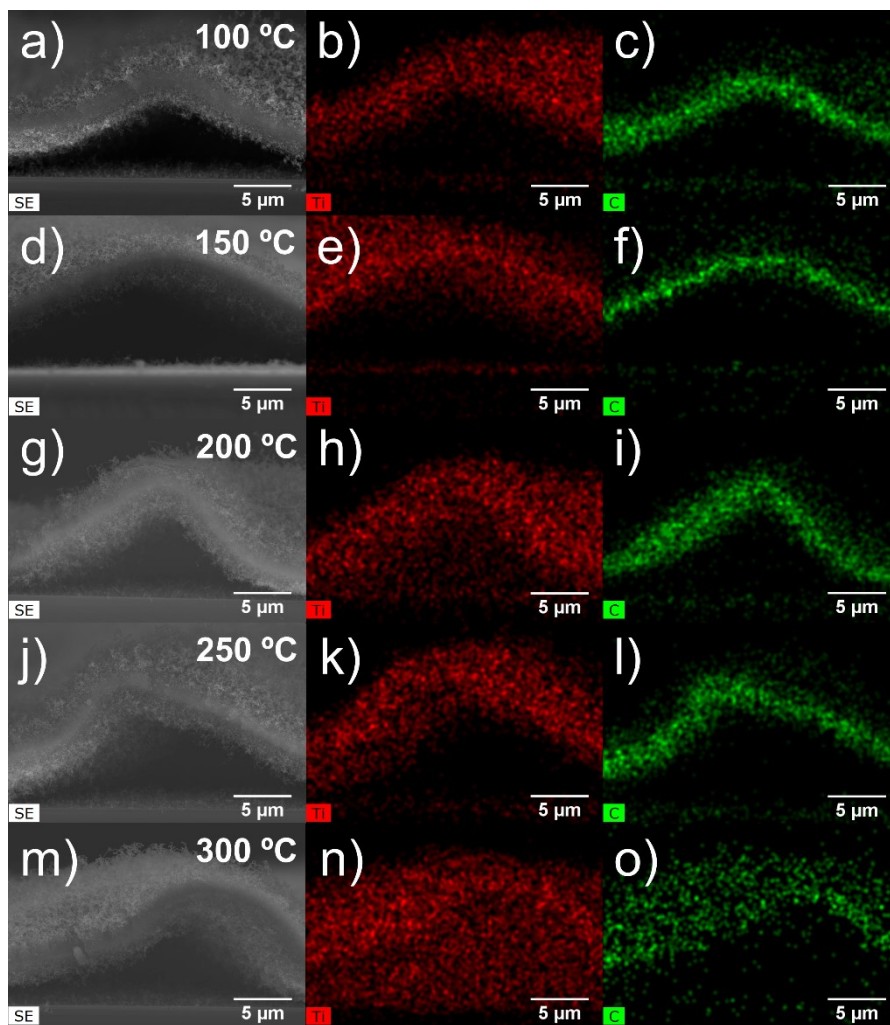
Figure S5. Cross-sectional SEM images and corresponding EDS elemental maps of the Ti and C from the TiO$_2$/w-VA-CNTs nanocomposites after 200 ALD cycles at different deposition temperatures. The elemental maps indicate a homogeneous Ti distribution within the VA-CNTs arrays at μm-scale.

Table S1. Estimated Ti/C ratio (at.%) values f maps indicate a homogeneous rom the SEM/EDS analysis.

| Sample | Deposition temperature (°C) | Ti/C (at.%) |
|---|---|---|
| w-VA-CNTs | 100 (200 cycles) | 1.725±0.032 |
| w-VA-CNTs | 150 (200 cycles) | 1.178±0.042 |
| w-VA-CNTs | 200 (200 cycles) | 0.923±0.043 |
| w-VA-CNTs | 250 (200 cycles) | 0.922±0.011 |
| w-VA-CNTs | 300 (200 cycles) | 0.274±0.002 |
| w-VA-CNTs | 300 (400 cycles) | 0.855±0.036 |
| VA-CNTs | 200 | 0.710±0.064 |

The average Ti/C ratio values and corresponding errors were obtained from acquiring three EDS spectra at different locations for each TiO$_2$/w-VA-CNTs nanocomposites (1 cm × 1 cm) after 200 ALD cycles at different deposition temperatures. For all samples, the error values are less than 1%, indicating the Ti good uniformity on the CNTs surface, corroborated by the SEM/EDS elemental mapping in Figure S5.
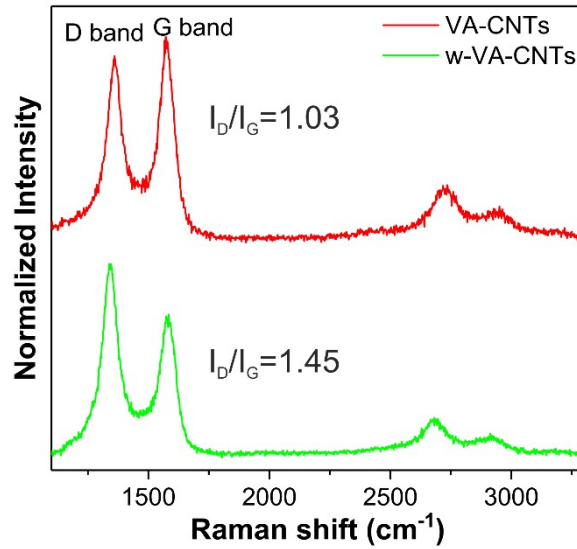
Figure S6. Raman spectra of w-VA-CNTs and VA-CNTs and corresponding $I_D/I_G$ ratio values. The $I_D/I_G$ value of 1.45 means a higher degree of disorder or defects on the w-VA-CNTs. It is well known that this type of defects on carbon nanotubes can act as nucleation sites for $TiO_2$ ALD growth.

Table S2. Raman peak position of D and G bands.

| Sample | D Band ($cm^{-1}$) | G Band ($cm^{-1}$) | $I_D/I_G$ |
|---|---|---|---|
| w-VA-CNTs (650°C) | 1342.27 | 1578.99 | 1.45 |
| VA-CNTs (700°C) | 1360.21 | 1574.65 | 1.03 |

The observed differences in the $I_D/I_G$ value arise from the deposition temperature of the TCVD process, higher deposition temperatures lead to a lower degree of disorder or defects.
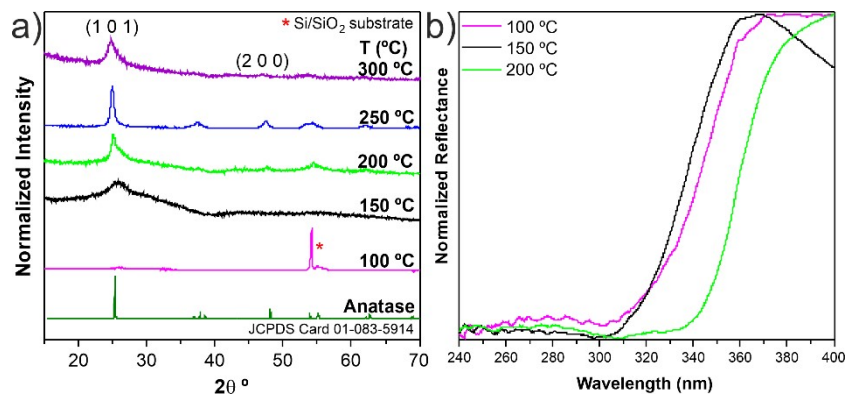


Figure S7. Representative GIXRD diffraction patterns (a), UV-vis diffuse reflectance spectra (b) of the $TiO_2$/w-VA-CNTs nanocomposites after 200 ALD cycles at different deposition temperatures. The absence of $TiO_2$ related GIXRD peaks at 100 °C confirms that the structure of the films is amorphous. The * denotes the diffraction peak of Si/SiO$_2$ substrate.

5

Table S3. Estimated crystallite size.

| Sample | Deposition temperature (°C) | Crystallite size (nm) |
|---|---|---|
| TiO$_2$/w-VA-CNTs | 100 (200 cycles) | -- -- |
| TiO$_2$/w-VA-CNTs | 150 (200 cycles) | 2.43 |
| TiO$_2$/w-VA-CNTs | 200 (200 cycles) | 13.77 |
| TiO$_2$/w-VA-CNTs | 250 (200 cycles) | 13.64 |
| TiO$_2$/w-VA-CNTs | 300 (200 cycles) | 4.60 |
| TiO$_2$/w-VA-CNTs | 300 (400 cycles) | 34.33 |
| TiO$_2$ - P25 | -- -- | 22.62 |

The crystallite size was calculated using the Debye–Scherrer equation from the main diffraction peak (101).

Table S4. Raman peak position and FWHM of anatase TiO$_2$/w-VA-CNTs after 200 ALD cycles at different deposition temperatures.

| Sample | $E_{g(1)}$ | |
|---|---|---|
| Deposition temperature (°C) | Position (cm$^{-1}$) | FWHM (cm$^{-1}$) |
| 150 | 147.1 | 23.7 |
| 200 | 148.5 | 17.9 |
| 250 | 147.8 | 17.0 |
| 300 | 149.4 | 26.2 |
| TiO$_2$ - P25 | 143.4 | 14.0 |

In order to better evaluate the differences between the spectra, the wavenumbers and the full width at half maximum (FWHM) of the Raman modes are summarized in Table S4. The dominant low-frequency mode of anatase TiO$_2$ around 148 cm$^{-1}$ is associated with the O-Ti-O bonding vibration ($E_{g(1)}$).
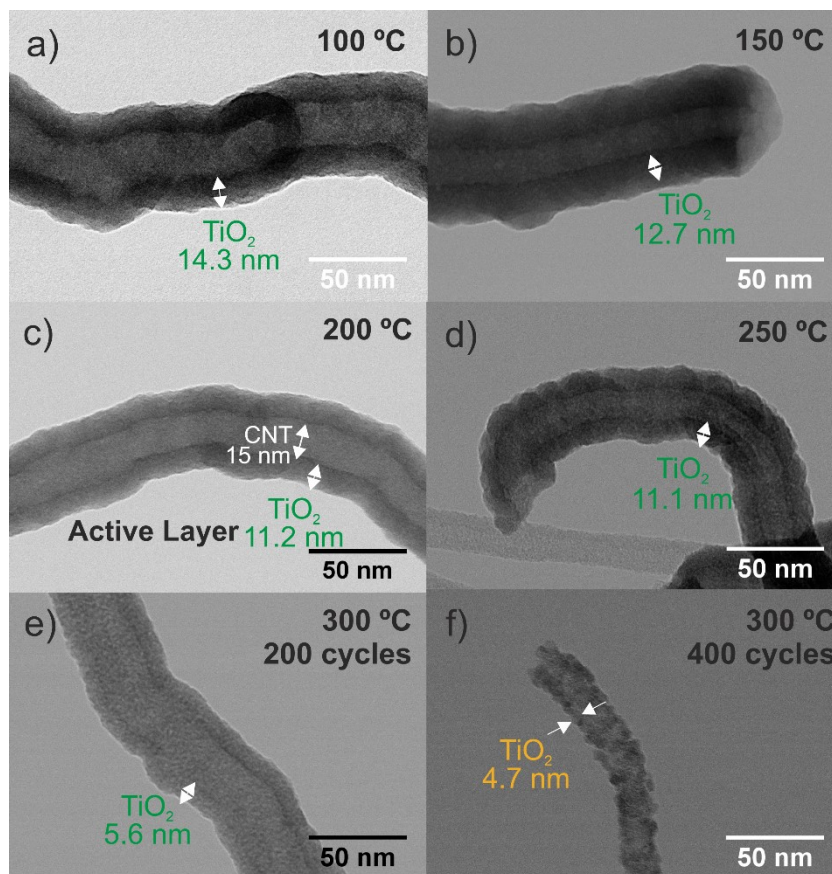
Figure S8. Representative TE-STEM mode images of coated nanotubes (w-VA-CNTs arrays) with $TiO_2$ after 200 ALD cycles at (a) 100 °C, (b) 150 °C, (c) 200 °C, (d) 250 °C, (e) 300° C and a nanotube coated with $TiO_2$ after 400 ALD cycles at 300 °C (f).
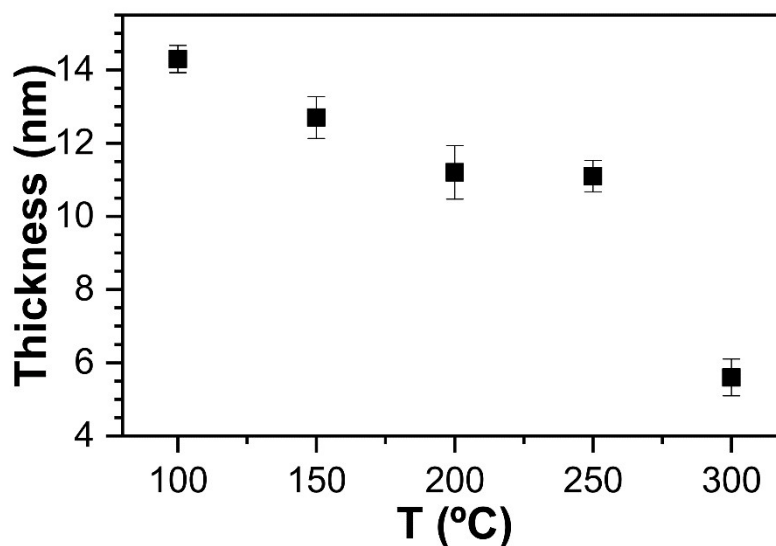


Figure S9. Thickness of $TiO_2$ thin films as a function of the deposition temperature. The thickness is estimated from the $TiO_2$ thin film thickness measured after 200 ALD cycles on w-VA-CNTs from TE-STEM mode images (Figure S8). Error bars indicate the standard deviation. It can be observed that a good saturation feature is attained when the deposition temperature was varied from 200 to 250 °C. The $TiO_2$ thin films were deposited with 200 ALD cycles at a fixed condition of 0.5 s TTIP pulse, 20 s of residence time, 10 s Ar purging, 2 s $H_2O$ pulse, 15 s of residence time, and 10 s Ar purging.

Table S5. Estimated growth rate values (*i.e.,* growth per cycle, GPC).

| Sample | Deposition temperature (°C) | Thickness (nm) | GPC (nm) |
|---|---|---|---|
| w-VA-CNTs | 100 (200 cycles) | 14.3 | 0.072 |
| w-VA-CNTs | 150 (200 cycles) | 12.7 | 0.063 |
| w-VA-CNTs | 200 (200 cycles) | 11.2 | 0.056 |
| w-VA-CNTs | 250(200 cycles) | 11.1 | 0.055 |
| w-VA-CNTs | 300 (200 cycles) | 5.6 | 0.028 |
| w-VA-CNTs | 300 (400 cycles) | 4.7 | 0.012 |
| Si (100) | 200 (200 cycles) | 17.7 | 0.088 |

The film growth per cycle (GPC) was calculated by dividing the film thickness by the total number of ALD cycles. At a deposition temperature of 200 °C, the growth rate of $TiO_2$ thin film is slightly larger on Si substrate. The $TiO_2$ film thickness on Si substrate determined by XRR was inserted for comparison.
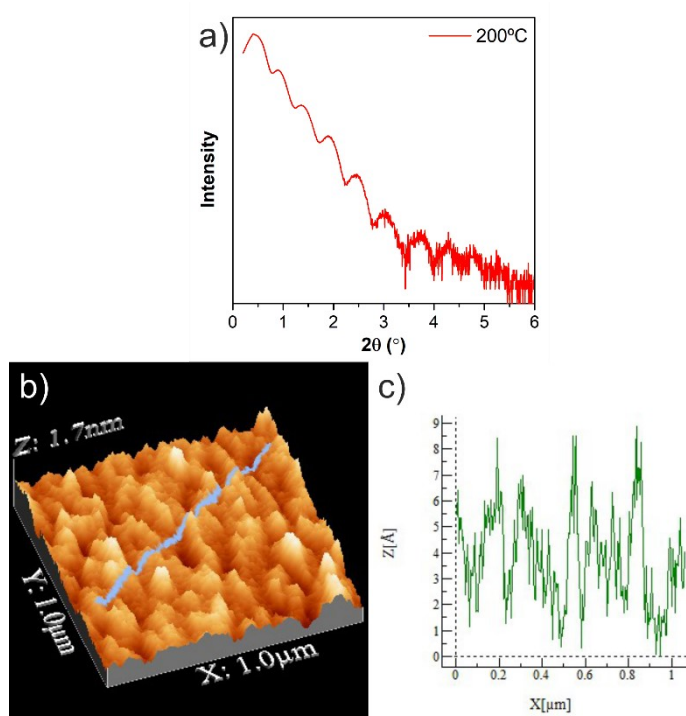


Figure S10. XRR pattern (a), 3D rendered AFM topography images (1 μm × 1 μm) (b), and corresponding height profile (c) along the blue line shown in (b) of the $TiO_2$ thin film after 200 ALD cycles at 200 °C onto Si substrates. From the XRR, the film thickness is estimated to be 17.7 nm and the roughness (RMS) value is 0.21 nm, determined from the AFM image. The film is very uniform with RMS roughness of less than 1.2% for its thickness.

Table S6. Summary of growth rates of $TiO_2$ films deposited by ALD, using TTIP and $H_2O$ precursors, on nanotubes.

| Ti precursor | O₂ precursor | T (°C) | TiO₂ Phase | GPC (Å/cycle) | Substrate | Observations/Application | Ref. |
|---|---|---|---|---|---|---|---|
| TTIP | $H_2O$ | 60<br>120<br>220 | Amorphous<br>Anatase inclusions<br>Anatase | 0.16<br>0.27<br>0.65 | VA-CNTs<br>(150 µm) | Non-functionalized | (1) |
| TTIP | $H_2O$ | 160<br>200<br>240 | Amorphous<br>Amorphous + Anatase | 0.26 | MWCNTs and pre-treated | Crystallinity depends on number of cycles | (2) |
| TTIP | $H_2O$ | 60 | Amorphous | 0.33 | VA-CNTs | Post annealing 450 °C, 30 min<br>Ultrafiltration membranes | (3) |
| TTIP | $H_2O$ | 150<br>250 | Amorphous<br>Anatase | 0.29<br>0.40 | CNTs<br>Oxidation in nitric acid | | (4) |
| TTIP | $H_2O$ | 250 | Anatase | 0.15 | Treated CNTs<br>Si substrate | Lithium ion batteries | (5) |
| TTIP | $H_2O$ | 100-300 | Amorphous<br>Anatase | 0.6 | w-VA-CNTs<br>(2.3 µm) | Non-functionalized<br>Photocatalysis | This work |

Figure S11. XPS survey spectra of (a) uncoated w-VA-CNTs and (b) TiO$_2$/w-VA-CNTs after 200 ALD cycles at 200 °C. The XPS survey spectrum of the uncoated w-VA-CNTs is also plotted as a reference. The main peak is attributed to the graphitic carbon of the nanotubes.
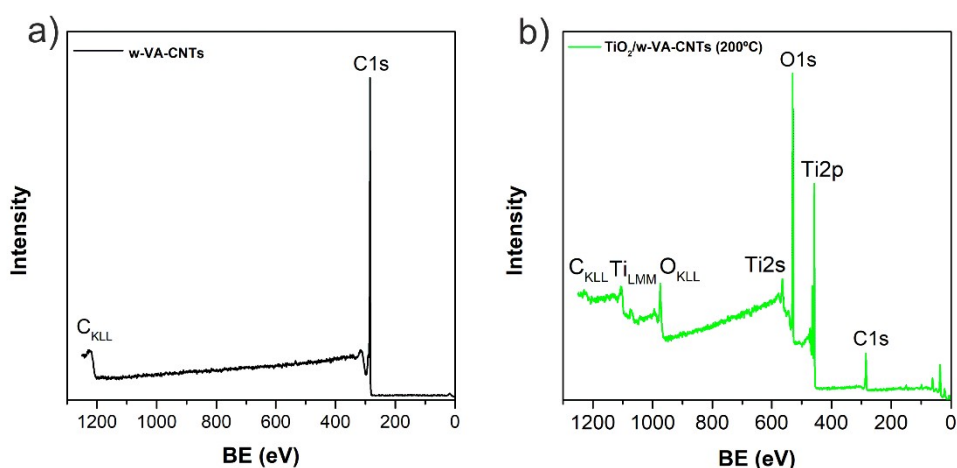


Table S7. XPS peak fit data components for Ti 2p and O 1s core-level spectra related to TiO$_2$ deposited at 200 °C, after 200 ALD cycles (GL - % of Lorentzian peak shape character).

| Ti 2p | Position (eV) | FWHM (eV) | Area (a.u.) | GL (%) |
|---|---|---|---|---|
| Ti 2p$_{3/2}$ | 458.2 | 1.1 | 71117.2 | 19 |
| Ti 2p$_{1/2}$ | 463.9 | 2.0 | 35558.6 | 23 |
| O 1s | Position (eV) | FWHM (eV) | Area (a.u.) | GL (%) |
| O-Ti | 529.8 | 1.2 | 77970.5 | 0 |
| Ti-OH | 532.5 | 1.2 | 14644.3 | 100 |

For confirmation, the atomic ratio of Ti:O, considering only low-binding energy O 1s peak and summation over all Ti 2p related peaks. Ti atoms in the Ti$^{4+}$ state, thus confirming the growth of TiO$_2$ on the surface.

Table S8. Atomic ratio Ti:O estimation for TiO$_2$.

| | RSF | Area of peaks | Atomic ratio Ti:O |
|---|---|---|---|
| Ti 2p$_{3/2}$ | 5.22 | 71117.2 | |
| Ti 2p$_{1/2}$ | 2.59 | 35558.6 | 0.51 |
| O 1s (O-Ti) | 2.93 | 77970.5 | |

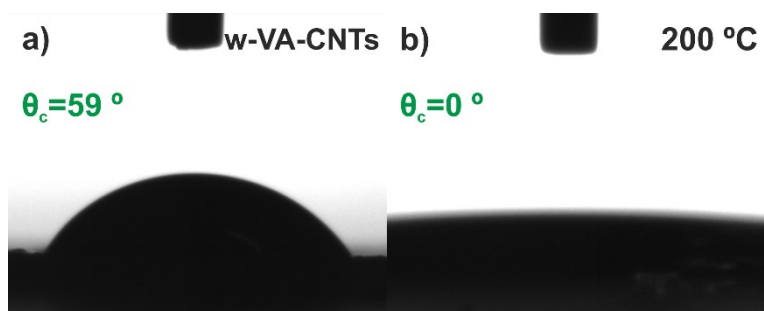RSF stands for relative sensitivity factor for each element.



Figure S12. Water contact angle (WCA) of uncoated w-VA-CNTs (a) TiO$_2$ coated w-VA-CNTs at 150 °C (b) and 200 °C (c). As the water contact angles are less than 90°, the surfaces become hydrophilic, in general. Anatase TiO$_2$ film grown at 200 °C presents a hydrophilic surface with a water contact angle of ~0°, a thin water-film is observed. A hydrophilic surface is favorable to enhanced photocatalytic performance of the RhB in aqueous solution.

Figure S13. Cross-sectional SEM images and corresponding EDS elemental maps of the Ti and C from the TiO$_2$/w-VA-CNTs (a) and the TiO$_2$/VA-CNTs (d) nanocomposites after 200 ALD cycles at 200 °C.
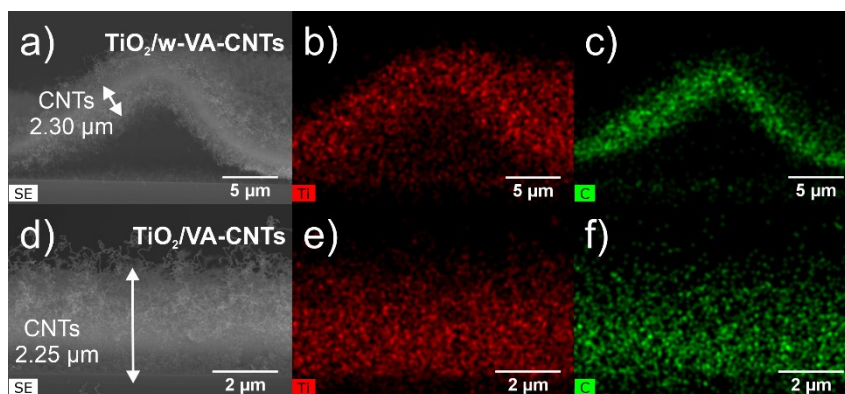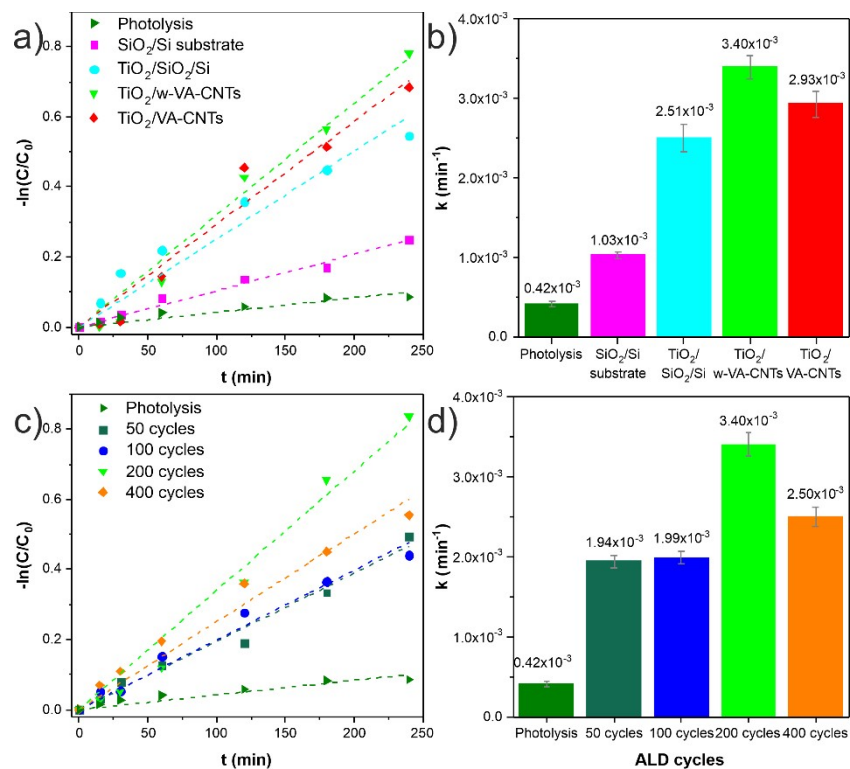
Figure S14. The time profiles of -ln(C₀/C) under UV–Vis irradiation for degradation of RhB aqueous solution and photocatalytic degradation percentage (%) of RhB with different types of substrates with 200 ALD cycles (a,b) and the number of ALD cycles (c,d). The deposition temperature was 200 °C for all samples.



The line slope of $TiO_2$/w-VA-CNTs was the highest among the samples, which demonstrated the importance of nanostructured $TiO_2$ thin film (Figure S14a). From Figure S14c it can be seen that the pseudo-first-order rate constant increases with the number of ALD cycles reaching the highest value for 200 ALD cycles, pointing out the optimum loading of $TiO_2$.

Figure S15. Cross-sectional SEM images and corresponding EDS elemental maps of the Ti and C from the TiO$_2$/w-VA-CNTs nanocomposites before (a) and after photodegradation tests (4 cycles).
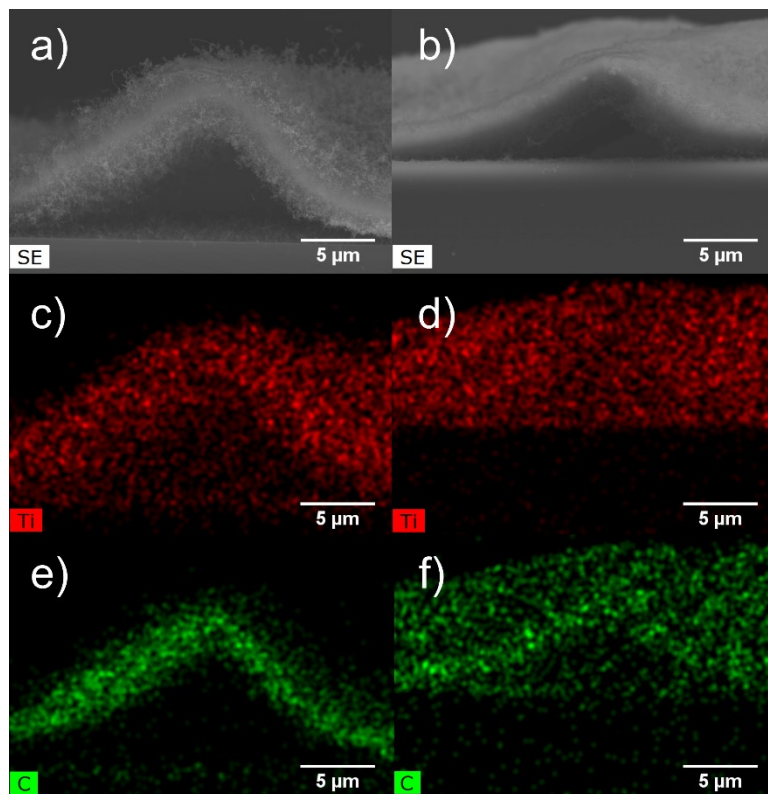


Table S9. Estimated Ti/C ratio (at.%) values from the SEM/EDS analysis.

| Sample | Deposition temperature (°C) | Ti/C (at.%) |
|---|---|---|
| w-VA-CNTs – Before (a) | 200 | 0.923±0.043 |
| w-VA-CNTs – After (b) | 200 | 0.807±0.073 |

The average Ti/C ratio values of $TiO_2$/w-VA-CNTs nanocomposite before and after the photodegradation tests, indicating that $TiO_2$ remains supported on the nanotube surface with good photostability for long-term use.

# References

1.      Guerra-Nuñez C, Zhang YC, Li M, Chawla V, Erni R, Michler J, et al. Morphology and crystallinity control of ultrathin $TiO_2$ layers deposited on carbon nanotubes by temperature-step atomic layer deposition. Nanoscale. 2015;7(24):10622-33.
2.      Zhang YC, Guerra-Nuñez C, Utke I, Michler J, Rossell MD, Erni R. Understanding and Controlling Nucleation and Growth of $TiO_2$ Deposited on Multiwalled Carbon Nanotubes by Atomic Layer Deposition. Journal of Physical Chemistry C. 2015;119(6):3379-87.
3.      Feng JH, Xiong S, Wang ZG, Cui ZL, Sun SP, Wang Y. Atomic layer deposition of metal oxides on carbon nanotube fabrics for robust, hydrophilic ultrafiltration membranes. Journal of Membrane Science. 2018;550:246-53.
4.      Meng XB, Geng DS, Liu JA, Li RY, Sun XL. Controllable synthesis of graphene-based titanium dioxide nanocomposites by atomic layer deposition. Nanotechnology. 2011;22(16):10.
5.      Wang BQ, Liu J, Sun Q, Xiao BW, Li RY, Sham TK, et al. Titanium Dioxide/Lithium Phosphate Nanocomposite Derived from Atomic Layer Deposition as a High-Performance Anode for Lithium Ion Batteries. Advanced Materials Interfaces. 2016;3(21):1600369.